RSC Advances

PAPER

View Article Online
View Journal | View Issue

Cite this: *RSC Adv.*, 2015, **5**, 85019

Solution processed nanomanufacturing of SERS substrates with random Ag nanoholes exhibiting uniformly high enhancement factors†

Ritu Gupta,‡[ad] Soumik Siddhanta,‡[b] Gangaiah Mettela,‡[a] Swati Chakraborty,[a] Chandrabhas Narayana[b] and Giridhar U. Kulkarni§*[ac]

Received 24th August 2015
Accepted 24th September 2015

DOI: 10.1039/c5ra17119a

www.rsc.org/advances

Achieving high Raman enhancement (SERS) that is relatively uniform over a large substrate area has been a major challenge in nanomanufacturing, as enhancement is localized around a plasmonic hotspot and hotspots are not usually spread uniformly over a substrate. Herein, we demonstrate a single-step, scalable method for the fabrication of Ag nanohole-based SERS substrates exhibiting $\sim 10^8$ enhancement factors. The SERS enhancement of these substrates could be further augmented by approximately 4 times through interference effects involving an underlying SiO_2 spacer of controlled thickness on the Si substrate, in agreement with FDTD simulations. Electrical activation by applying a short DC pulse across the Ag film and Si substrate resulted in ~12% additional increase in the enhancement factor, while importantly the standard deviation of the signal across the 1 cm^2 substrate decreased from 9.5% to 3.1%. Both these effects could be attributed to electromigration of the metal producing protrusions on the nanoparticle surfaces thus populating with the hotspots for high performance SERS. These relatively uniform and reproducible SERS-chips with high enhancement factors can potentially be used as highly sensitive multi-functional platforms for point-of-care diagnostics.

1. Introduction

Plasmonic nanomaterials have the unique ability to confine far-field propagating light into an optical near-field, resulting in the localization of surface plasmons and creation of a strong electromagnetic field.[1] The field is further enhanced when isolated nanoparticles come together and their plasmons are coupled resulting in hotspot formation.[2] These hotspots may be harnessed to enhance the Raman scattering intensity from the probe molecules located in the vicinity of the nanostructures, which is the familiar Surface Enhanced Raman Spectroscopy (SERS).[3] Thus, SERS provides molecular fingerprints at ultralow analyte concentrations down to single molecule detection, with cross-sections comparable to fluorescence probes.[4] Due to such high sensitivity, SERS is being used in sensors and spectroscopic applications.[5,6] Several two dimensional (2D) nanostructured SERS substrates based on highly ordered nanopillars,[7] nanoholes,[8] nanodiscs,[9] nanorings,[10] and nanopetals[11] prepared using gold or silver have been fabricated with high enhancement factors (*G*-factors). Complex 3D-nano/microstructures such as nanoparticles in well-defined holes,[12] bowls[13] or cups,[14] corrugated bipyramidal microcrystallites[15] and roughed surfaces[16] have been explored. While many such structures produce appreciable SERS enhancement,[17] the reproducibility and uniformity of performance, however, remain the foremost challenges standing in the way of tapping the full capability of SERS in real world applications. This is particularly important, for instance, when collecting metabolic profiles across considerably large areas of tissue cross-section.[18] The only way out is to design well defined plasmonic substrates with uniform enhancement over a large area.[19] In this direction,

[a]*Thematic Unit of Excellence on Nanochemistry and Chemistry and Physics of Materials Unit, Jawaharlal Nehru Centre for Advanced Scientific Research (JNCASR), Jakkur P.O., Bangalore 560064, India. E-mail: kulkarni@jncasr.ac.in*

[b]*Light Scattering Laboratory, Chemistry and Physics of Materials Unit, Jawaharlal Nehru Centre for Advanced Scientific Research (JNCASR), Jakkur P.O., Bangalore 560064, India*

[c]*Centre for Nano and Soft Matter Sciences, Jalahalli, Bangalore 560013, India*

[d]*Department of Chemistry, Indian Institute of Technology Jodhpur, Jodhpur-342011, Rajasthan, India*

† Electronic supplementary information (ESI) available: The supporting information contains: a large area photograph of the SERS substrate; SEM images of Ag patterned on a textured Si surface; UV-vis spectra of the Ag films with different heating rates; SERS enhancement factor calculations; Raman mapping of the Ag film; Raman spectra of the Ag film without holes; cross-sectional SEM images of the Ag films on the SiO_2/Si substrates with different SiO_2 thicknesses; histogram showing the reproducibility of the SERS substrate over multiple samples; UV-vis spectra of the Ag/SiO_2 (100 nm)/Si and Ag/SiO_2 (300 nm)/Si and Ag/SiO_2 (500 nm)/Si substrates; electric field intensity distribution over the Ag/SiO_2 (100 nm)/Si and Ag/SiO_2 (500 nm)/Si substrates; bar graph showing the mean and maximum electric field intensities for the Ag/SiO_2/Si substrates with variable SiO_2 thicknesses; XRD showing the oxidation of the Ag film; bar graph showing the SERS intensities after application of a 5 V bias on the Ag/SiO_2 (300 nm)/Si substrate. See DOI: 10.1039/c5ra17119a

‡ These authors have contributed equally.

§ On lien from JNCASR Bangalore-560064, India.

several efforts have been made, for example, a thin SiO_2 layer coated on nanoparticles was shown to enable uniformity in SERS signals.[20] Bhuvana and Kulkarni fabricated a patterned substrate where the metal nanostructure could be controlled to produce a constant SERS signal.[21] However, there is a dire need to develop cost effective substrates.

In this work, we have utilized nanocrystalline Ag films with random nanoholes to achieve uniform, reproducible SERS substrates with high *G*-factors. Hole Enhanced Raman Spectroscopy (HERS) has emerged as a powerful spectroscopic tool.[22] Periodic hole arrays have been associated with highly intense electromagnetic fields due to the extraordinary optical transmission and localized surface plasmons ideally required for SERS.[23] The electromagnetic enhancement contribution in SERS[24] is due to the localized surface plasmons circumscribing the holes. The hole structure gives rise to interesting plasmonic effects which can be harnessed effectively for SERS-based applications.[18] Usually, periodic nanohole arrays are fabricated using complicated and expensive lithographic processes like electron beam lithography[25] and focused ion beam lithography.[26] Other techniques combining phase-shift lithography, template development and etching, electron beam deposition and lift-off,[27] UV-nanoimprint lithography[28] and ion etching have also been used to make nanohole arrays.[29] There are several known disadvantages with lithographic techniques such as multiple step processing, and these steps are usually time intensive and expensive due to the use of masks with limited sizes. Nanosphere lithography is an inexpensive method that can generate periodic hole patterns; however, the local variations and defects over extended areas make it somewhat unreliable for large areas.[30] However, random holes prepared using a simple colloidal lithography method have been shown to exhibit interesting optical properties.[31] It is important to note that the plasmonic effects arising from localized modes inside the hole are characteristic of the individual hole itself, independent of whether the hole is in a periodic array or a set of randomly distributed holes.[32] For SERS or any other plasmonic application in general, it is highly desirable to develop nanomanufacturing methods that can be used for the fabrication of such nanoholes with ultimate uniformity and reproducibility which is otherwise difficult to achieve with low throughput and limited area nanolithography techniques. To be commercially viable, it is imperative that the fabrication procedure is cost and time effective and devoid of sophisticated instrumentation.

Herein, we have developed a precursor-based, fast and single-step fabrication strategy to fabricate random nanoholes in a Ag film as a SERS substrate. Ag ink has previously been employed to make transparent conducting electrodes on flexible substrates for solar cell fabrication, however not much attention was given to the surface plasmons from these random hole type nanostructures.[33,34] The SERS substrates were created by simply coating a Ag precursor ink and decomposing it by heating at a nominal temperature of 130 °C resulting in a Ag film hosting randomly distributed nanoholes. Furthermore, we have increased the SERS enhancement by introducing a SiO_2 spacer layer between the holes and the Si substrate thereby trapping the light. Interestingly, we have also been able to increase the particle coupling controllably by bias induced electrical activation. Thus the fabricated Ag nanohole substrates exhibit $\sim 10^8$ SERS enhancement with a variation of only 3% thanks to the dense network of hotspots over a wide area.

2. Experimental

2.1 Fabrication of random Ag nanoholes

n-Si and n-Si/SiO_2 (of 100, 300 and 500 nm SiO_2 thickness), textured Si, glass and flexible PET substrates were used for this study. The Ag ink precursor (SC-100, 20 wt%, Kunshan Hisense Electronics Co., Ltd, China) was diluted by adding 4 times the volume of isopropanol and sonicated for 15 min in dark ambient conditions. The resulting solution was filtered with a 0.45 μm size PTFE Whatman filter. The Ag ink can be painted using a brush as shown in the schematic in Fig. 1, however, 100 μL of Ag ink was spin coated for 45 s at 2000 rpm on pre-cleaned Si and Si/SiO_2 substrates for reproducibility. The decomposition of Ag ink to Ag was carried out by heating inside an oven at 130 °C for 10 min.

2.2 Characterization

The morphology of Ag was analyzed in air using atomic force microscopy (AFM) equipment (Di Innova SPM, Bruker) under contact mode using standard cantilevers. Scanning electron microscopy (SEM) imaging was done using a Nova NanoSEM 600 instrument (FEI Co., The Netherlands). The reflection spectra were collected using an integrating sphere with a Perkin-Elmer Lambda 900 UV/visible/near-IR spectrophotometer. The Raman and the SERS spectra were recorded in the 180° backscattering geometry, using a 532 nm excitation from a diode pumped frequency doubled Nd:YAG solid state laser (model GDLM-5015 L, Photop Suwtech Inc.) and a custom-built Raman spectrometer[35] equipped with a SPEX TRIAX 550 monochromator and a liquid nitrogen cooled CCD (Spectrum One with CCD 3000 controller, ISA Jobin Yvon). Laser power at the sample was ≈8 mW, and a typical spectral acquisition time was 5 s. Prior to acquiring SERS spectra, the substrate was dipped in thiophenol solution (0.1 mM) for 4 h and washed with water and ethanol to remove unbound molecules. Thiophenol was used to calculate the SERS enhancement factor (G) using the method given by Yu *et al.*:[36] $G = (I_{SERS}/I_{NORM})(N_{BULK}/N_{SURF})$ where I_{SERS} and I_{NORM} are the intensities of a specific band in the SERS and normal Raman spectra of the analyte molecule, respectively. N_{BULK} and N_{SURF} are the number of probe molecules which are illuminated under the laser beam in bulk and SERS experiments, respectively. N_{SURF} is given by CA, where C and A are the surface densities of thiophenol (6.8×10^{14} molecules cm^{-2})[37] and the laser spot area (~ 4 μm^2), respectively. N_{BULK} is given by $Ah\rho/m$, where h, ρ, and m are the penetration depth (100 μm), the density (1.079 g cm^{-3}), and the molecular weight (110.18 g mol^{-1}) of thiophenol, respectively. The calculated values are tabulated in Note S2.†

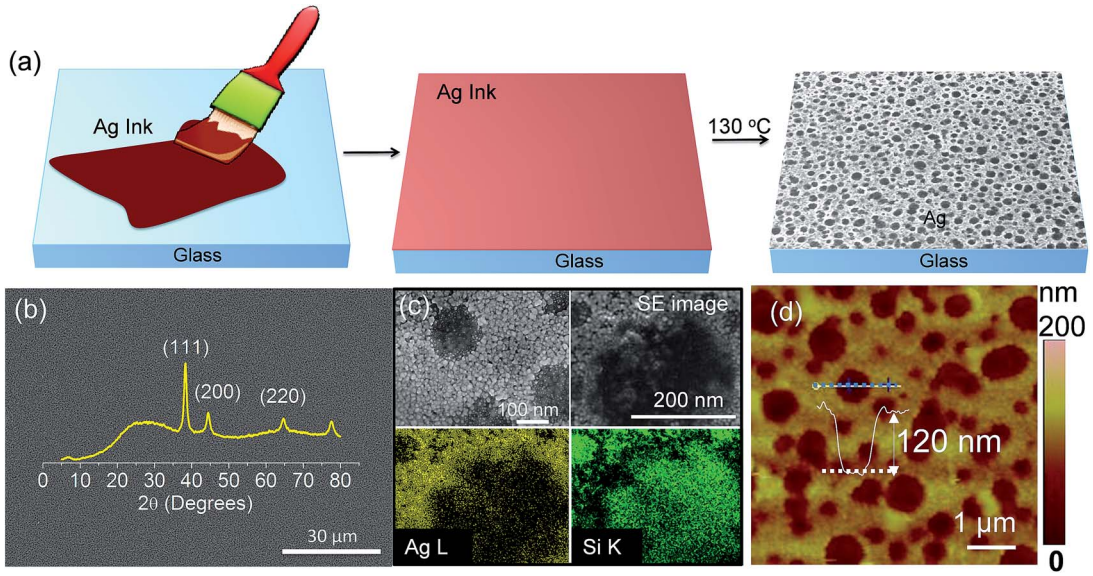

Fig. 1 (a) Schematic demonstrating the fabrication of the Ag film, (b) SEM image with a bird's eye view of the Ag film with an overlaid XRD pattern, (c) magnified SE image of a hole and the corresponding EDS signal maps of Ag L and Si K, and (d) a typical AFM image of the perforated Ag film with the inset showing the cross-section profile of the hole along the blue dotted line.

2.3 Finite-difference time domain (FDTD) simulations

FDTD simulations (Lumerical Solutions Ltd) were used to determine the near-field intensities at the interface of the silver films and the glass/silicon substrate. To simulate the surface, AFM topography images of the Ag nanoholes were used. The simulation zone consists of periodic boundary conditions along the x and y axes, and along the z axis perfectly matched layers (PML) were introduced to absorb the waves moving out of the zone and hence preventing reflection from the boundaries. A plane-wave polarized light of wavelength 532 nm was used along the y-axis. For minimum simulation time and to maximize the field enhancement resolution, the mesh override region was set to 0.5 nm, and the overall simulation time was 100 fs.

3. Results and discussion

3.1 Fabrication of random Ag nanoholes

The simple fabrication process for the formation of the perforated Ag metallic film on a glass/PET substrate is schematically described in Fig. 1a. Briefly, Ag precursor ink is coated on the substrate and the wet film is rapidly decomposed by heating on a hotplate preset at 130 °C, not allowing self-drying of the volatile solvent. The commercial Ag precursor was purposefully diluted with isopropanol to cause dewetting of the precursor film. The SEM images in Fig. 1b and S1† show large area views of the Ag film. The XRD pattern overlaid in Fig. 1b shows that the Ag ink, upon decomposition, yields polycrystalline Ag without any oxide phase. The peaks are rather broad due to the nanometric size of the particles; the size estimated from the Scherrer formula is ~10 nm (see ESI, Note S1 for the calculations†). Interestingly, the Ag film was observed to be perforated with random holes of ~500 nm in size, which formed due to dewetting of the precursor during solvent evaporation and decomposition (Fig. 1c). EDS mapping (see Fig. 1c) corresponding to the Ag L signal shows the presence of Ag metal nanoparticles at the edges except for a few small nanoparticles in the middle. The Si K signal seen in the middle emphasizes that the holes run deep down to the glass surface. As seen from the AFM image in Fig. 1d, the Ag film is granular with interconnected Ag nanoparticles of ~20–50 nm in size. The height profile across a hole shows the depth to be around 120 nm.

The formation of a hole type structure due to dewetting of colloidal films while drying is known in the literature.[38] As the solvent evaporates, a random set of holes open up in the precursor film with a receding contact line due to dewetting. The nanoparticles formed by the decomposition of the precursor are driven towards the rim of the holes until a sufficient number of nanoparticles have accumulated to pin the receding contact line leading to hole formation. With the present method, perforated Ag films can be prepared over indefinitely large areas, the size being limited only by the size of the heating source. This is a relatively simple method compared to lithography techniques where large area patterning is always a challenge. Additionally, unlike lithography methods, here the formation of holes is nearly independent of the surface roughness, as holes are observed to form on textured surfaces as well (see Fig. S2†).

3.2 Optimization of random nanoholes

The size and distribution of the holes can be tuned by carrying out the Ag precursor decomposition at different ramping rates (Fig. 2). As seen from the SEM images, there are significant variations in the hole size and density with a change in the decomposition conditions. The Ag film exhibits holes everywhere formed with isolated nanoparticles. Image J analysis was

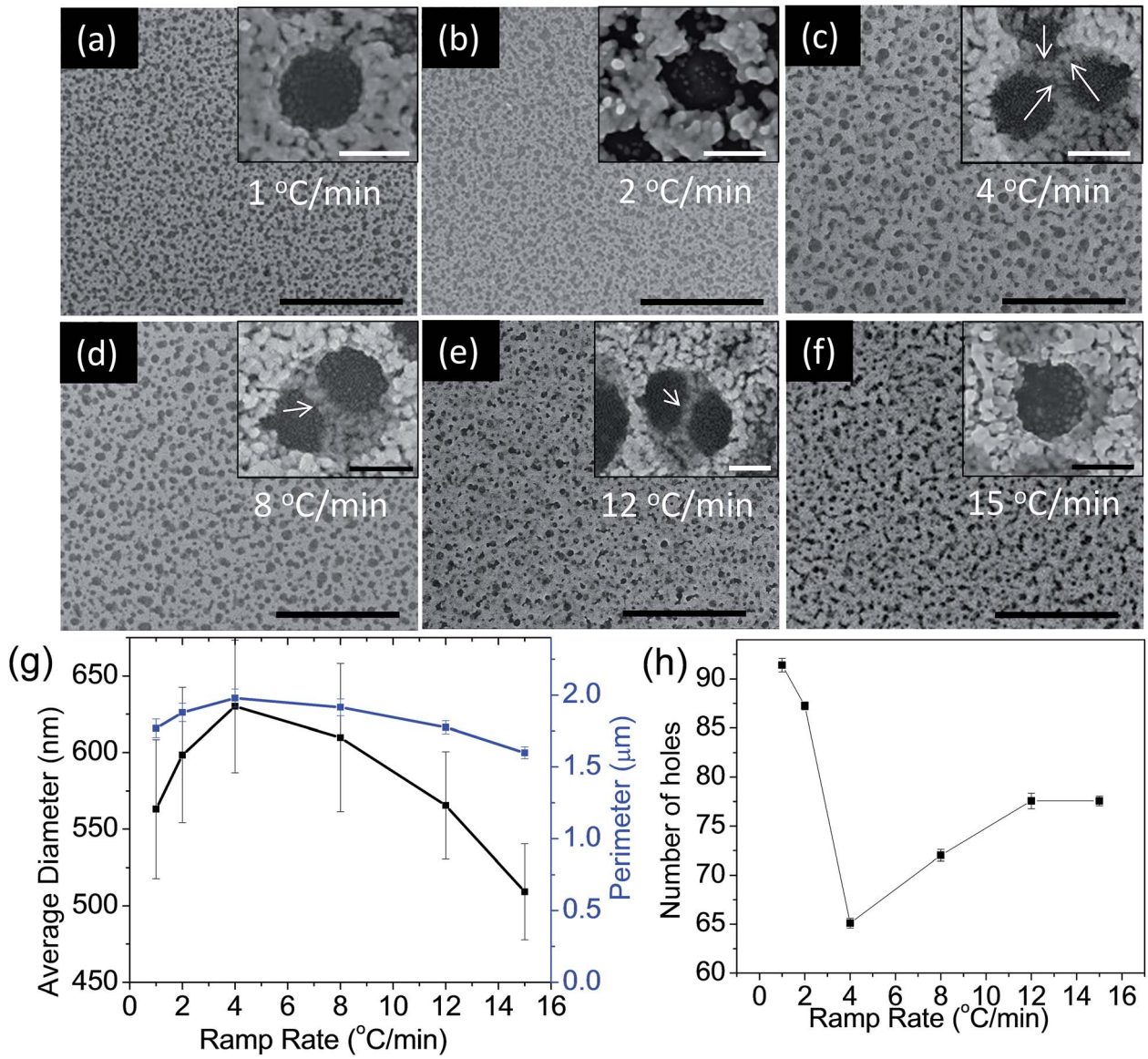

Fig. 2 (a–f) SEM images of the Ag films prepared at ramp rates of 1, 2, 4, 8, 12 and 15 °C min^{-1}, respectively. Scale bars at the bottom are 10 μm. Insets show higher magnification views of a representative nanohole with scale bars of 400 nm. Plots showing (g) the average hole diameter and corresponding perimeter, and (h) holes per mm^2 as a function of the decomposition ramp rate. Note that the error bars are calculated using average values from the SEM images in (a–f). Areas of ~700 μm^2 were considered to count the number of holes.

performed to estimate the size and number of holes using SEM images taken at the same magnification. The average diameter and area of the holes prepared at a 1 °C min^{-1} ramp rate are ~0.55 ± 0.04 μm (Fig. 2a) and 0.23 ± 0.001 μm^2, respectively. The film prepared at 2 °C min^{-1} appears to be similar to that at 1 °C min^{-1}, however, the magnified image in Fig. 2b shows that the nanoparticles at the periphery of the holes have reduced interconnectivity. The decomposition at 4 °C min^{-1} (Fig. 2c) shows several secondary holes infused in each submicron/micron hole. This significantly increases the size of the primary hole with greater edge sites thus increasing the overall perimeter of the holes. It is interesting that the nature of the holes is sensitive to the temperature ramp rate, with the final annealing temperature being the same in all cases. As the ramp rate influences the rate of solvent evaporation, this is understandable. However, the mechanism for the formation of the secondary holes is not very clear, and is probably associated with the ramp dependent release of gaseous products upon decomposition of the organic precursor. At higher ramp rates of 8, 12 and 15 °C min^{-1}, the hole density increases and the diameter gradually decreases (Fig. 2d–f), perhaps due to insufficient time for hole formation. These trends have been captured in the plots in Fig. 2g and h. The hole diameter varied between 500 and 830 nm as the temperature ramp varied between 1 and 15 °C min^{-1}. Significantly large error bars in the plot indicate polydispersity in the size of the holes. The optical spectra corresponding to the films show a broad band with a slight variation in the maximum plasmon wavelength

(Fig. S3†). The absorption at the maximum plasmon wavelength with respect to the incident wavelength is a minimum indicating an enhanced interaction of light within the holes. The larger sized holes hosting secondary nanoholes produced using a 4 °C min^{-1} decomposition rate seem to be optimal for achieving enhanced plasmon coupling.

3.3 Random nanoholes as SERS substrates

SERS was performed on the perforated Ag films using thiophenol (TP) as the analyte. TP forms a monolayer on the Ag nanogranular surface *via* stable Ag–S bonds and does not evoke any interfering fluorescence background facilitating an unambiguous enhancement calculation. Its bonding to the metal surface is confirmed by the decrease in frequency of the in-plane ring breathing mode coupled to the ν(C–S) mode from 1092 to 1069 cm^{-1}. In the SERS spectra measured for the Ag films prepared at different ramping rates (Fig. 3a), the peak at 1470 cm^{-1} corresponds to the Ag–S band from the thiolate bonding. Other peaks at 1066, 1017 and 996 cm^{-1} can be assigned to the in-plane phenyl ring stretching band, in-plane ring deformation, and in-plane ring deformation mode coupled to the S–H bending mode, respectively. The peak at 1572 cm^{-1} corresponds to the C–C stretching mode. The enhancement factor has been calculated using the 1572 and 996 cm^{-1} bands as shown in Fig. 3b. From the plots, it is clear that the 4 °C min^{-1} Ag film with larger holes and higher hole perimeter exhibits the highest enhancement factor. Ag films prepared under the same conditions (4 °C min^{-1}) produce reproducible SERS signals as shown in Fig. S4.† This film was further examined (Fig. 3c) for SERS in different locations. The variation in the intensity of the 996 cm^{-1} peak from 20 arbitrary locations (see Fig. 3d) is only 9.4% which indicates a high degree of uniformity of the film over a large area, which is rather uncommon among typical SERS substrates.[39,40] The uniformity in the SERS signal over a 25 × 25 μm^2 area can be seen from the Raman map in Fig. S5.† The specialty of our SERS platform is the presence of a rough and granulated silver surface interspersed with holes on a dielectric substrate, glass. Such a two dimensional metal–dielectric film can support surface plasmons, higher order multipolar plasmons as well as planar film waveguide modes[41] which get coupled to the random holes resulting in localized surface plasmons (LSPs). A thick Ag film without holes (control) exhibited a lower intensity signal and

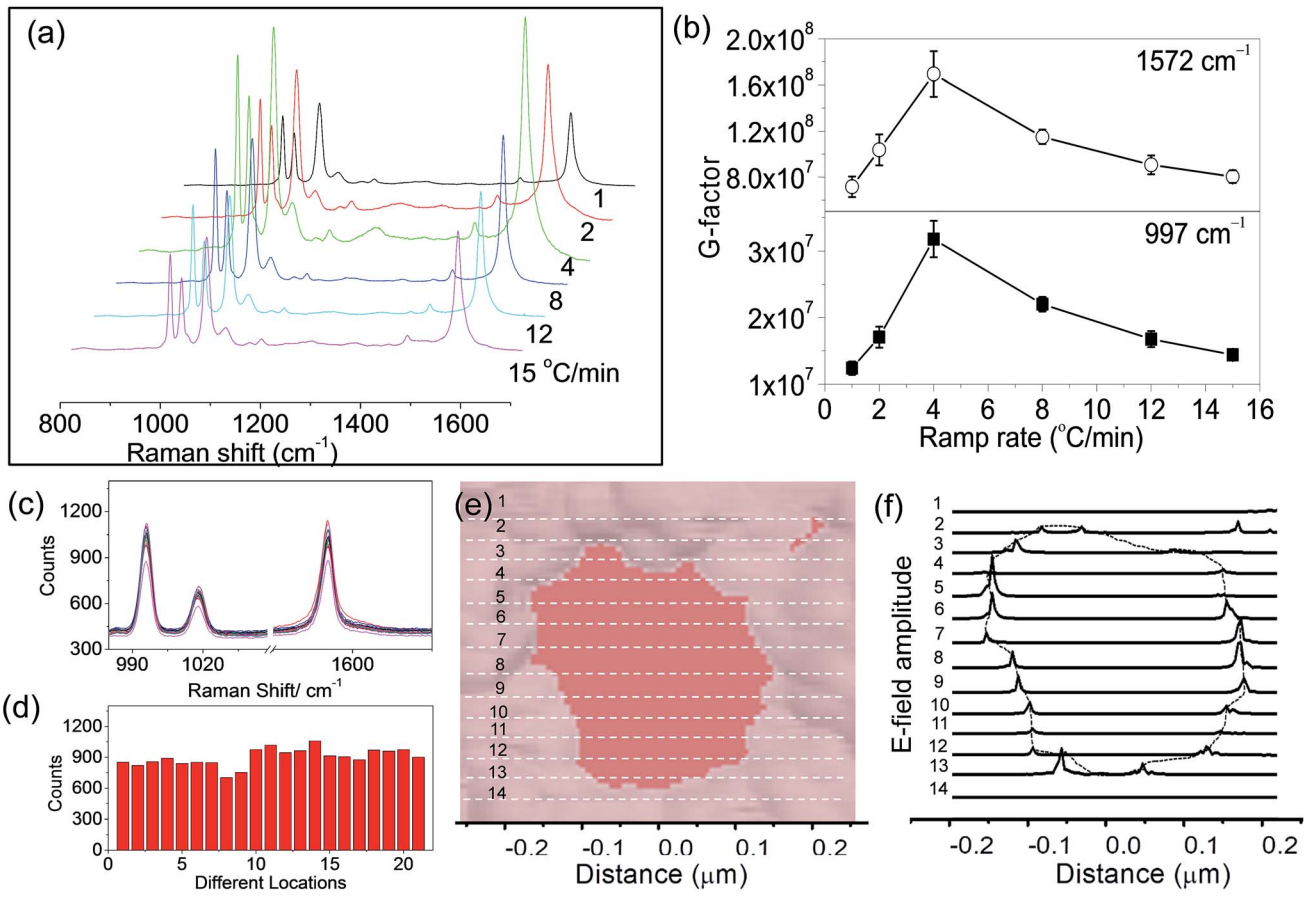

Fig. 3 (a) SERS spectra for the Ag films prepared with different ramp rates and (b) *G*-factors for the 996 and 1572 cm^{-1} modes of thiophenol (TP) adsorbed on the Ag films prepared with different ramp rates. (c) Raman spectra obtained from different locations of the Ag film prepared with a 4 °C min^{-1} ramp rate and (d) the corresponding SERS signal intensity distribution measured at 996 cm^{-1}. (e) 2D-FDTD simulation set up using an AFM topography image of a Ag nanohole on a Si substrate. The dotted lines indicate the positions where the *E*-field intensity is calculated. (f) *E*-field intensity along the lines marked in (e).

correspondingly a 5 times lower *G*-factor (Fig. S6†). The randomness of the holes that induces the nanoscale heterogeneity is known to enhance the *G*-factor values.[42,43] FDTD simulations were performed to study the effect of random nanoholes on the electric near field intensities in the Ag films. Fig. 3e shows the image of an irregular Ag void (detailed in the Experimental section) with the *E*-field profiles presented in Fig. 3f. As seen from the figure, the highest *E*-field intensity is found at the edges of the void, reminiscent of localized surface plasmons (LSPs). This analysis also explains why the 4 °C min^{-1} prepared Ag film containing secondary hole structures with the lowest nanohole perimeter (see Fig. 2h) has a relatively higher *G*-factor.

3.4 SERS enhancement by optical interference effects

It is known that plasmonic nanostructures when overlaid on a dielectric medium lead to strong enhancements due to electromagnetic wave trapping.[44,45] Thus, Ag holes can be utilized to induce light trapping as schematically represented in Fig. 4a. Dielectric SiO_2 layers of different thicknesses were introduced in between the reflective Si substrate and the Ag film to facilitate light trapping within the voids. Thus, Ag/SiO_2 (100 nm)/Si, Ag/SiO_2 (300 nm)/Si and Ag/SiO_2 (500 nm)/Si films were prepared (see cross sectional SEM images in Fig. S7†) to study the effect of thickness on light trapping; in all cases, a decomposition ramp rate of 4 °C min^{-1} was employed, as it showed a relatively higher absorption (see ESI Fig. S3†). The UV-vis spectrum (Fig. 4b) shows the plasmonic modes corresponding to the Ag/SiO_2 (300 nm)/Si film. The absorption over a broad range, 500 to 800 nm, is seen to be distinctly different from the spectra obtained with Ag films hosted on 100 and 500 nm SiO_2 layer thicknesses and is also different compared to the spectra from Ag/Si and Ag/glass (see Fig. S8†). The spectrum obtained from the substrate devoid of Ag film (SiO_2 (300 nm)/Si) shows much less absorption compared to the broad peak in the 500–800 nm region in the case of Ag. This in turn may be taken to indicate that in the Ag/

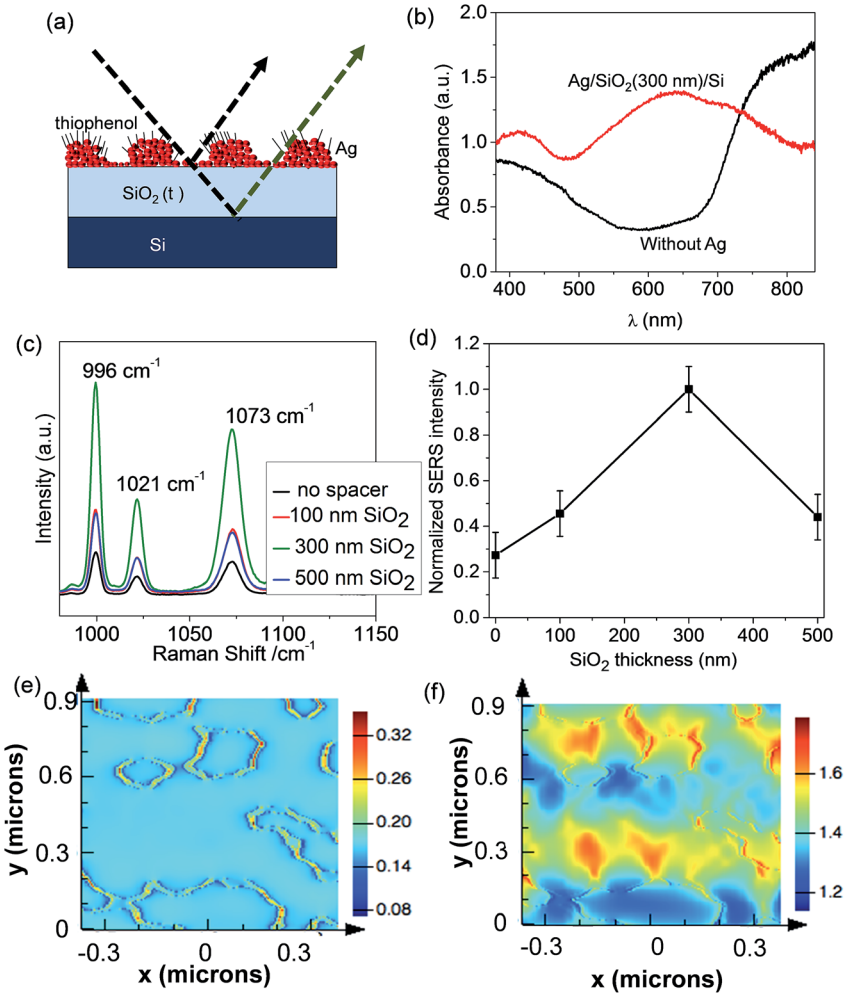

Fig. 4 (a) Schematic illustrating the interference effect in the perforated Ag film hosted on the SiO_2/Si substrate. (b) UV-visible spectra of the perforated Ag film on the SiO_2 (300 nm)/Si substrate (red) along with the blank substrate (black). (c) Raman spectra of thiophenol for Ag films on Si/SiO_2 with different thicknesses of the SiO_2 layer. (d) Variation in the normalized SERS intensity corresponding to the 996 cm^{-1} band with respect to the SiO_2 layer thickness. Note that the error bars in (d) have been calculated from 5 different locations. Electric field intensity maps of (e) Ag/Si and (f) Ag/SiO_2 (300 nm)/Si.

SiO_2 (300 nm)/Si film, a considerable amount of visible light gets transmitted through the holes to the underlying SiO_2/Si thus enhancing the overall absorption. The penetrated light undergoes multiple reflections leading to interference and enhancement of the near field electromagnetic field intensity at the Ag/SiO_2 interface. However, due to this broad spectral nature, the contributions due to transmission from holes, surface plasmons and interference effects are hard to distinguish.

The Ag/SiO_2 (300 nm)/Si substrate shows a relatively high light trapping effect as it facilitates constructive interference. The interference law is denoted by the equation, $a = \eta d/\lambda$; where η is the refractive index, d is the thickness of the SiO_2 dielectric layer and λ is the wavelength of the laser used. The value of a is a sinusoidal function with a peak value at $a = (2m + 1)/4$ where m is a natural number. The value of a is maximum at 300 nm which is also evident in the FDTD calculations discussed below. As seen in Fig. 4c and d, at 532 nm excitation wavelength, the enhancement factor in the case of Ag/SiO_2 (300 nm)/Si is ~4 times higher relative to that of the plain Ag/Si substrate. The enhancement in the case of Ag/SiO_2 (300 nm)/Si is also more than that of the Ag/SiO_2 (100 nm)/Si and Ag/SiO_2 (500 nm)/Si substrates which is therefore consistent with the superior interference based light trapping effect in the 300 nm SiO_2 spacer layer. The presence of a resonant cavity between the nanoporous Ag film and the Si surface *via* the SiO_2 layer is thus evident.

FDTD simulations were performed to study the optical interference arising from surface plasmons and the porous nanostructures in the Ag films laid on the SiO_2/Si substrate. The intensity distribution maps shown in Fig. 4e and f correspond to the electric field intensity $|E|^2$ obtained from the FDTD simulations performed using the AFM image of a Ag nanohole. Without the SiO_2 layer (Fig. 4e), the electric field intensity is higher at the hole edges similar to the situation seen in Ag/glass (see Fig. 3c and d). However, as the spacer layer (300 nm) is introduced, the electric field intensity becomes much stronger and extends in the ridges connecting the holes (Fig. 4f) probably due to random interference and multiple scattering by the nanoholes. Above and below 300 nm, the average electric field intensity is lowered (see Fig. S9 and S10†) which is also consistent with the trend seen in the SERS enhancement. Thus

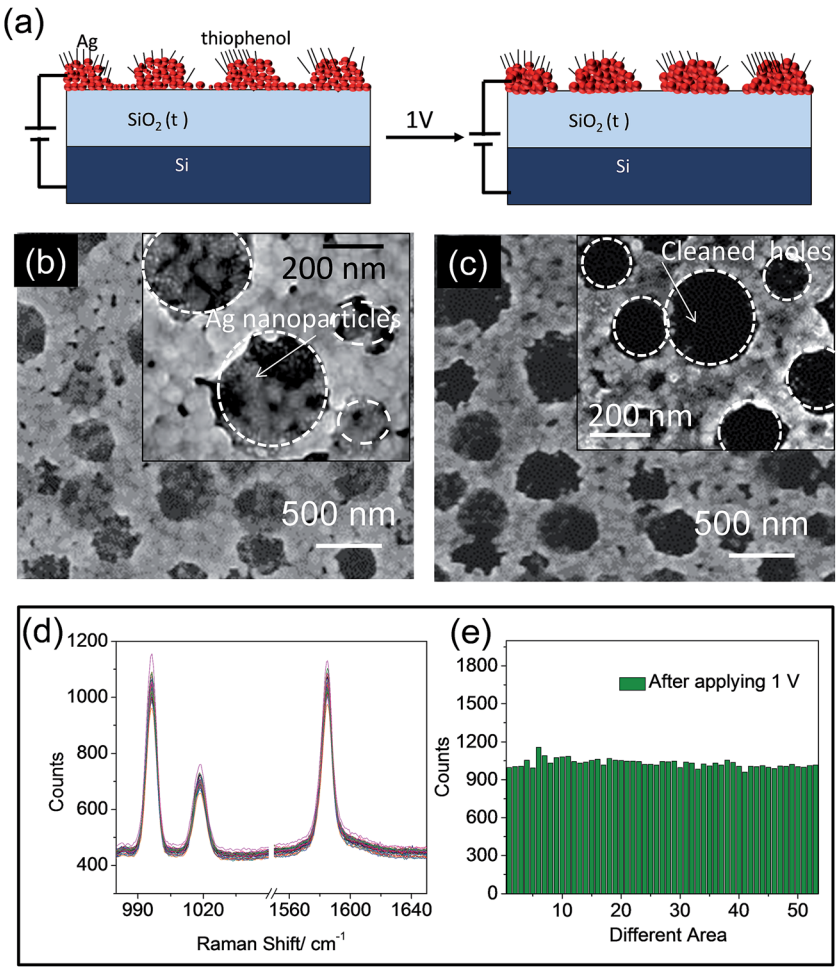

Fig. 5 (a) Schematic demonstrating the effect of the application of an electric field on the Ag/SiO_2 (300 nm)/Si substrate. (b and c) SEM images before (pristine) and after applying 1 V across the Ag film and Si substrate with a dielectric spacer. (d and e) Raman spectra over a 1 cm^2 area from different locations after electrical activation and its SERS signal (at 996 cm^{-1}) intensity distribution.

for the 532 nm light used, a dielectric spacer layer of ~300 nm seems to be optimum for enhancing the SPR by interference effects. Our observations are also consistent with the interference-enhanced SERS signals reported in the literature for graphene, ITO nanoparticles and Ag nanoparticles.[46–48]

3.5 Electrical activation for relatively uniform SERS

While enhancement factors up to 10^8 to 10^9 have been achieved in highly aggregated systems[49] as well as in controlled nanoparticle aggregation systems[50] due to the presence of 'hotspots' at specific locations, issues relating to substrate reproducibility and uniformity often remain unattended.[51] Although the Ag films with random holes show high SERS signals, smaller Ag nanocrystals present in the voids lead to a standard deviation of 9.49% of the enhancement factor as seen previously in Fig. 3b. Such non-uniformity, though relatively small in this case, can arise due to varied inter-particle coupling in the film. One way out is to anneal the film so as to controllably increase the particle coupling while not seriously affecting its roughness, the latter being a prerequisite to obtain SERS enhancement. In this work, we have performed controlled electrical activation of the Ag/SiO_2 (300 nm)/Si substrate akin to the electrode based SERS enhancement strategies in the early days of SERS.[52] A nominal voltage bias of 1 V was applied across the Ag film and Si substrate for 10 s as shown schematically in Fig. 5a followed by recording the SERS signal. The effect of electrical activation is discernible in the SEM images as well as in the SERS signal. The SEM images in Fig. 5b and c show that the holes became well-defined and the inter-particle connectivity was also improved. The Ag nanoparticles present on the ridges across the voids get annealed as a result of the electrical activation. The voids become clear and free of small Ag nanocrystals as the latter coalesced into the nanogranular film. The SERS signal shown in Fig. 5d following electrical activation amounts to an ~12% higher enhancement factor (Fig. 5e), but importantly has a standard deviation of 3.17% which is nearly one-third that of the pristine film (see Fig. 3b). Thus, the method of electrical activation, by applying a bias across the dielectric layer with the top Ag film and bottom Si electrodes, improved the SERS performance dramatically. Applying a bias across the Ag film for Joule heating of the film leads to a decrease in the sheet resistance due to annealing but does not improve SERS (see Fig. S11†). External heating is also not advisable as it results in uncontrolled oxidation of the Ag nanoparticle surface (see ESI, Fig. S12†). The method of electrical activation chosen here causes mild Joule heating. The observed effect may primarily be attributed to electrostriction-enabled electromigration of Ag that may produce innumerable small but sharp protrusions on the nanoparticle surfaces thus increasing the surface roughness and local hotspots. However, on further increasing the voltage, the SERS signal decreased due to increased coupling between nanoparticles on account of possible annealing (see ESI, Fig. S13†). Interestingly, the high SERS enhancement factor (ranging between 10^7 and 10^8) and ultimate uniformity (relative variation, 3.1%) achieved with a tiny electrical activation (1 V) should already be suitable for commercialisation.

4. Conclusions

Ag films with random nanoholes have been fabricated covering 100 cm^2 areas using a single step solution process where hole formation was achieved by simply tuning the heating rate during the Ag precursor decomposition on glass or Si substrates. A rate of 4 °C min^{-1} was found to be optimal to produce a Ag film with a higher nanohole perimeter (~2.6 μm), which exhibited a relatively high SERS enhancement factor of the order of 10^7 to 10^8. FDTD simulations on the Ag film showed an enhanced electric field at the edges of the holes due to localized surface plasmons. Instead of using a bare Si substrate, a SiO_2/Si substrate with a 300 nm oxide layer was used to create light trapping interference effects and this gave rise to further enhancement of SERS. The electrical activation of the Ag film/SiO_2/Si substrate with a small bias not only further improved the signal but also ensured a relatively high uniformity of SERS over the substrate area. The high *G*-factors, and reproducible and uniform SERS originating from these Ag films with nanoholes make them ideally suitable for commercial applications. Being a lithography-free technique, and combined with the ability for scale-up, this method holds great promise for detection technologies.

Acknowledgements

The authors thank Nanomission DST, India for generous support. The authors thank Prof. C. N. R. Rao for his constant encouragement. R. G. acknowledges JNCASR for postdoctoral fellowship. G. M. thanks CSIR, India for financial assistance.

References

1 L. Novotny and N. van Hulst, *Nat. Photonics*, 2011, **5**, 83–90.
2 W. Zhou and T. W. Odom, *Nat. Nanotechnol.*, 2011, **6**, 423–427.
3 S. L. Kleinman, R. R. Frontiera, A.-I. Henry, J. A. Dieringer and R. P. van Duyne, *Phys. Chem. Chem. Phys.*, 2013, **15**, 21–36.
4 K. Kneipp, H. Kneipp, R. Manoharan, I. Itzkan, R. R. Dasari and M. S. Feld, *Bioimaging*, 1998, **6**, 104–110.
5 D. Karthigeyan, S. Siddhanta, A. H. Kishore, S. S. R. R. Perumal, H. Ågren, S. Sudevan, A. V. Bhat, K. Balasubramanyam, R. K. Subbegowda, T. K. Kundu and C. Narayana, *Proc. Natl. Acad. Sci. U. S. A.*, 2014, **111**, 10416–10421.
6 S. Siddhanta, V. Thakur, C. Narayana and S. M. Shivaprasad, *ACS Appl. Mater. Interfaces*, 2012, **4**, 5807–5812.
7 J. D. Caldwell, O. Glembocki, F. J. Bezares, N. D. Bassim, R. W. Rendell, M. Feygelson, M. Ukaegbu, R. Kasica, L. Shirey and C. Hosten, *ACS Nano*, 2011, **5**, 4046–4055.
8 S. H. Lee, K. C. Bantz, N. C. Lindquist, S.-H. Oh and C. L. Haynes, *Langmuir*, 2009, **25**, 13685–13693.
9 Q. Yu, P. Guan, D. Qin, G. Golden and P. M. Wallace, *Nano Lett.*, 2008, **8**, 1923–1928.
10 M. G. Banaee and K. B. Crozier, *Opt. Lett.*, 2010, **35**, 760–762.

11 C. S. Rout, A. Kumar, G. Xiong, J. Irudayaraj and T. S. Fisher, *Appl. Phys. Lett.*, 2010, **97**, 133108.
12 H. Wei, U. Håkanson, Z. Yang, F. Höök and H. Xu, *Small*, 2008, **4**, 1296–1300.
13 T. Bhuvana and G. U. Kulkarni, *Nanotechnology*, 2009, **20**, 045504.
14 F. M. Huang, D. Wilding, J. D. Speed, A. E. Russel, P. N. Bartlett and J. J. Baumberg, *Nano Lett.*, 2011, **11**, 1221–1226.
15 G. Mettela, R. Boya, D. Singh, G. V. P. Kumar and G. U. Kulkarni, *Sci. Rep.*, 2013, **3**, 1793.
16 G. Mettela and G. Kulkarni, *Nano Res.*, 2015, 1–10.
17 G. Mettela, S. Siddhanta, C. Narayana and G. U. Kulkarni, *Nanoscale*, 2014, **6**, 7480–7488.
18 S. Yamazoe, M. Naya, M. Shiota, T. Morikawa, A. Kubo, T. Tani, T. Hishiki, T. Horiuchi, M. Suematsu and M. Kajimura, *ACS Nano*, 2014, **8**, 5622–5632.
19 W. Xu, X. Ling, J. Xiao, M. S. Dresselhaus, J. Kong, H. Xu, Z. Liu and J. Zhang, *Proc. Natl. Acad. Sci. U. S. A.*, 2012, **109**, 9281–9286.
20 J. F. Li, Y. F. Huang, Y. Ding, Z. L. Yang, S. B. Li, X. S. Zhou, F. R. Fan, W. Zhang, Z. Y. Zhou, Y. WuDe, B. Ren, Z. L. Wang and Z. Q. Tian, *Nature*, 2010, **464**, 392–395.
21 T. Bhuvana and G. U. Kulkarni, *Small*, 2008, **4**, 670–676.
22 J. T. Bahns, Q. Guo, J. M. Montgomery, S. K. Gray, H. M. Jaeger and L. Chen, *J. Phys. Chem. C*, 2009, **113**, 11190–11197.
23 T. W. Ebbesen, H. J. Lezec, H. F. Ghaemi, T. Thio and P. A. Wolff, *Nature*, 1998, **391**, 667–669.
24 P. G. Etchegoin and E. C. le Ru, in *Surface Enhanced Raman Spectroscopy*, Wiley-VCH Verlag GmbH & Co. KGaA, 2010, pp. 1–37, DOI: 10.1002/9783527632756.ch1.
25 A. R. Hajiaboli, B. Cui, M. Kahrizi and V.-V. Truong, *Phys. Status Solidi A*, 2009, **206**, 976–979.
26 M. Najiminaini, F. Vasefi, B. Kaminska and J. J. L. Carson, *Opt. Express*, 2011, **19**, 26186–26197.
27 E.-S. Kwak, J. Henzie, S.-H. Chang, S. K. Gray, G. C. Schatz and T. W. Odom, *Nano Lett.*, 2005, **5**, 1963–1967.
28 F. Hamouda, G. Barbillon, S. Held, G. Agnus, P. Gogol, T. Maroutian, S. Scheuring and B. Bartenlian, *Microelectron. Eng.*, 2009, **86**, 583–585.
29 S. Rauf, M. J. A. Shiddiky, A. Asthana and K. Dimitrov, *Sens. Actuators, B*, 2012, **173**, 491–496.
30 P. Colson, C. Henrist and R. Cloots, *J. Nanomater.*, 2013, **2013**, 19.
31 T. H. Reilly, R. C. Tenent, T. M. Barnes, K. L. Rowlen and J. van de Lagemaat, *ACS Nano*, 2010, **4**, 615–624.
32 K. L. van der Molen, K. J. K. Koerkamp, S. Enoch, F. B. Segerink, N. F. van Hulst and L. Kuipers, *Phys. Rev. B: Condens. Matter Mater. Phys.*, 2005, **72**, 045421.
33 R. Gupta, M. Hösel, J. Jensen, F. C. Krebs and G. U. Kulkarni, *J. Mater. Chem. C*, 2014, **2**, 2112–2117.
34 M. Hösel and F. C. Krebs, *J. Mater. Chem.*, 2012, **22**, 15683.
35 G. V. P. Kumar and C. Narayana, *Curr. Sci.*, 2007, **93**, 778–781.
36 H.-Z. Yu, J. Zhang, H.-L. Zhang and Z.-F. Liu, *Langmuir*, 1999, **15**, 16–19.
37 A. D. McFarland, M. A. Young, J. A. Dieringer and R. P. van Duyne, *J. Phys. Chem. B*, 2005, **109**, 11279–11285.
38 P. C. Ohara and W. M. Gelbart, *Langmuir*, 1998, **14**, 3418–3424.
39 T. Wang, Z. Zhang, F. Liao, Q. Cai, Y. Li, S.-T. Lee and M. Shao, *Sci. Rep.*, 2014, **4**, 4052.
40 X. Liu, Y. Shao, Y. Tang and K.-F. Yao, *Sci. Rep.*, 2014, **4**, 5835.
41 J. M. Pitarke, V. M. Silkin, E. V. Chulkov and P. M. Echenique, *Rep. Prog. Phys.*, 2007, **70**, 1.
42 J. Biener, G. W. Nyce, A. M. Hodge, M. M. Biener, A. V. Hamza and S. A. Maier, *Adv. Mater.*, 2008, **20**, 1211–1217.
43 Y. Nishijima, J. B. Khurgin, L. Rosa, H. Fujiwara and S. Juodkazis, *Opt. Express*, 2013, **21**, 13502–13514.
44 L. C. T. Shoute, A. J. Bergren, A. M. Mahmoud, K. D. Harris and R. L. McCreery, *Appl. Spectrosc.*, 2009, **63**, 133–140.
45 G. Kumari and C. Narayana, *J. Phys. Chem. Lett.*, 2012, **3**, 1130–1135.
46 Y. Y. Wang, Z. H. Ni, Z. X. Shen, H. M. Wang and Y. H. Wu, *Appl. Phys. Lett.*, 2008, **92**, 043121.
47 D. Shan, L. Huang, X. Li, W. Zhang, J. Wang, L. Cheng, X. Feng, Y. Liu, J. Zhu and Y. Zhang, *J. Phys. Chem. C*, 2014, **118**, 23930–23936.
48 L. C. T. Shoute, *ChemPhysChem*, 2010, **11**, 2539–2545.
49 M. Cyrankiewicz, T. Wybranowski and S. Kruszewski, *J. Phys.: Conf. Ser.*, 2007, **79**, 012013.
50 J. Reboud, C. Auchinvole, C. D. Syme, R. Wilson and J. M. Cooper, *Chem. Commun.*, 2013, **49**, 2918–2920.
51 P. Pinkhasova, L. Yang, Y. Zhang, S. Sukhishvili and H. Du, *Langmuir*, 2012, **28**, 2529–2535.
52 D. D. Tuschel, J. E. Pemberton and J. E. Cook, *Langmuir*, 1986, **2**, 380–388.